Indian Journal of Chemistry
Vol. 56A, June 2017, pp. 592-600

Synthesis of α-Fe_2O_3 nanoparticles via wet high-energy ball-milling and its catalytic application in thermal decomposition of ammonium perchlorate

Seyed Ghorban Hosseini*, Esmaeil Ayoman & Azam Ghavi
Department of Chemistry, Malek Ashtar University of Technology, P.O. Box 16765-3454, Tehran, Iran
Email: hoseinitol@yahoo.com

Received 10 November 2016; revised and accepted 24 May 2017

α-Fe_2O_3 nanoparticles have been successfully produced by the wet high-energy ball-milling method. Phase and nanostructure characterizations of as-crushed powders have been done by X-ray diffraction and field emission scanning electron microscopy techniques. Average particle sizes of 56 and 51 nm are obtained after 20 and 40 hours of wet ball milling process, respectively. The catalytic property of the synthesised α-Fe_2O_3 nanoparticles in the thermal decomposition reaction of ammonium perchlorate has been evaluated by thermogravimetry and differential scanning calorimetry. Thermal analysis confirms that adding 5 wt.% α-Fe_2O_3 nanoparticles (51 nm) decreases the decomposition temperature of ammonium perchlorate from 422.0 °C to 360.0 °C and increases the ΔH of the decomposition reaction from 880 J g^{-1} to 1408.1 J g^{-1}. Finally, the catalytic effects of α-Fe_2O_3 NPs on kinetic and thermodynamic parameters of thermal decomposition reaction of treated AP particles have been studied by Kissinger, Boswell, Ozawa and Starink methods.

Keywords: Thermal decomposition, Kinetic parameters, Thermodynamic parameters, Nanoparticles, Wet high-energy ball-milling method, Ammonium perchlorate, Iron oxide

Solid propellants are commonly used as solid fuels for the propulsion of missiles and rockets[1,2]. High oxygen content and good thermal stability of chlorates and perchlorates have made them indispensable ingredients of pyrotechnics industry and key ingredients of solid propellants[3-5]. Ammonium perchlorate (AP) is the most widely used oxidizer for composite solid propellants since its thermal decomposition characteristics directly influence the combustion behavior of the propellant. The decomposition and burning rate of AP are mainly affected by variation of particle size or by the addition of catalysts, such as Nd_2O_3, α-Fe_2O_3, NiO, Co_3O_4, $NiCo_2O_4$, CuO, Mn_2O_3, $NiFe_{2-x}Cr_xO_4$, etc., which can decrease the decomposition temperature and increase burning rate and heat of decomposition[6-14]. It has been widely researched that α-Fe_2O_3 NPs can be applied for the catalytic decomposition of AP[7,15].

Iron oxide is widely studied and is of particular interest in technological applications such as gas sensor, catalysis, magnetic storage and etc.[16–18]. In order to synthesize Fe_2O_3 NPs, researchers have employed different chemical routes such as sol-gel processes[19], hydrothermal[20], solvothermal[21], and annealing[22] to obtain single phase Fe_2O_3 NPs. However, these methods are chemically intensive, require special equipments, external additives as stabilizers, high temperature and pressure, and substrate, and are difficult to scale for large scale synthesis since expensive and toxic chemicals are required, which may have adverse effects on medical and environmental applications[23]. Production of α-Fe_2O_3 NPs with respect to chemical purity, crystallinity, simplicity, phase selectivity, size homogeneity, and with controlled state of agglomeration using a cost effective method is still a challenge for material science scientists. Among these methods, wet high-energy ball-milling method is one of the simple, inexpensive, nontoxic, eco-friendly, efficient, and useful methods that can be easily scaled up for large scale to produce particle size of nanometer scale. Thus, large amounts of α-Fe_2O_3 NPs can be produced at a room temperature in a very efficient and useful process using this method[24,25]. The catalytic activity of chemically synthesized α-Fe_2O_3 NPs on the thermal decomposition of AP has been widely studied[3, 18-24]. However, there are no reports on the catalytic application of α-Fe_2O_3 NPs synthesized by high-energy ball-milling method for the thermal decomposition of AP particles.

The purpose of this research is to employ a simple, low-cost, fast and high yield method for the

production of extremely reactive α-Fe_2O_3 nanoparticles. The structural properties of the resulting α-Fe_2O_3 NPs have been characterized by X-ray diffraction (XRD) and scanning electron microscopy (SEM) techniques. We have also studied the performance of α-Fe_2O_3 NPs with different particle sizes as catalyst on the thermal decomposition of AP particles by differential scanning calorimetry and thermogravimetry analysis (DSC/TG). To the best of our knowledge, there is no report on the use of α-Fe_2O_3 NPs synthesized by high-energy ball-milling method as catalyst on the thermal decomposition of AP particles. All the α-Fe_2O_3 NPs revealed excellent catalytic performances. Further, the apparent activation energy of thermal decomposition processes of pure and treated samples have been obtained from DSC data experiments by the non–isothermal kinetic analysis method proposed by Kissinger, Bosswell, Ozawa and Starink. Also, the values of kinetic and thermodynamic parameters of the pure AP and nanocomposite of AP with α-Fe_2O_3 NPs (51 nm) have also been computed.

Materials and Methods

All chemicals including isopropyl alcohol (C_3H_8O) and methyl isobutyl ketone (MIBK, $C_6H_{12}O$) were purchased from Merck. AP (80-100 μm) and α-Fe_2O_3 (20-30 μm) microsize powders were purchased from Fluka.

The α-Fe_2O_3 (30 μm) powders were milled for 20 and 40 h using a Pulverisette-5 model Fritsch grinding machine Using four vertical grinding tungsten carbide vials, with inner volumes of 150 mL, placed on the sun wheel. X-ray diffraction (XRD) analysis was performed using a Philips PW 3710 X-ray powder diffractometer equipped with Cu Ka irradiation (λ = 1.5406 Å) at 2θ ranging from 0–90° with a step time of 0.5 s and a step size of 0.02°. Nanostructures characterizations of α-Fe_2O_3 nanoparticles produced in the grinding machine were investigated using FE-SEM (field emission scanning electron microscopy, HITACHI S-4160). The size and morphology of the AP+α-Fe_2O_3 nanocomposites were analyzed using FE-SEM (EIGMA/VP) coupled with energy dispersive spectroscopy (EDS). All thermal decomposition performances were investigated using STA-780 instrument at a temperature range of 25–500 °C and heating rate of 5, 10, 15 and 20 °C min^{-1} and under air atmosphere.

Synthesis of α-Fe_2O_3 NPs

The primary material α-Fe_2O_3 powder with a particle size of <30 μm were prepared at different milling time periods of 20 and 40 h. The powders were crushed using hardened tungsten carbide balls (10 mm dia.) to a powder ratio of 10:1 at a rotation speed of 150 rpm. Processing of the starting materials was carried out inside a glove box in order to protect the products from pollution. Also, a small amount of process control agent, i.e., isopropyl alcohol, was introduced into the jar together with the α-Fe_2O_3 powder and carbide balls. The α-Fe_2O_3 NPs prepared at a wet medium after 20 and 40 h, which are referred as FW20 and FW40 NPs.

Preparation of AP+α-Fe_2O_3 nanocomposites

Nanocomposite of AP+α-Fe_2O_3 was prepared using fast, novel, scalable, and low-cost solvent-nonsolvent method as detailed in a previous study[7].

In a typical experiment, for preparation of 1.0 g of AP+α-Fe_2O_3 nanocomposites (AP+5%FW40), AP (0.95 g) was dissolved in 10 mL water. Then, α-Fe_2O_3 NPs (FW40, 0.05 g) was dispersed in 25 mL MIBK using the ultrasonic apparatus for 20 min and then heated to 60-70 °C. In the third step to obtain AP+α-Fe_2O_3 nanocomposites, the saturated solution of AP was added dropwise to the α-Fe_2O_3 NPs solution and after several minutes of reaction, the AP was deposited on the surface of the α-Fe_2O_3 NPs. Finally, the coated particles (i.e., nanocomposites) were filtered and washed three times with 25 mL MIBK as a non-solvent, and dried at ambient temperature.

AP+α-Fe_2O_3 nanocomposites were prepared with varying mass percentage (2 and 5 wt.%) of α-Fe_2O_3 NPs. The choice of solvent is critical in solvent-nonsolvent method. In the present study, α-Fe_2O_3 NPs must be insoluble and AP soluble in the selected solvent system. Herein, MIBK and water were selected as the nonsolvent and solvent system, respectively.

Results and Discussion

Characterization of α-Fe_2O_3 NPs

The crystallinity of the typically synthesized α-Fe_2O_3 NPs was determined by XRD (Fig. 1 (a-b)). As shown in the XRD pattern of the FW20 NPs (Fig. 1a), all of the diffraction peaks are in well agreement with the rhombohedral phase (space group *R*3*c* and space group number 167) of hematite (ICSD 01-089-2810) with cell constants of $a = b = 5.04$ Å, $c = 13.75$ Å, $\alpha = \beta = 90.00$, and $\gamma = 120.00$. It can be seen in the XRD pattern of the FW40 NPs (Fig. 1b) that all the diffraction peaks are well matched with the standard rhombohedral (space group *R*3*c* and

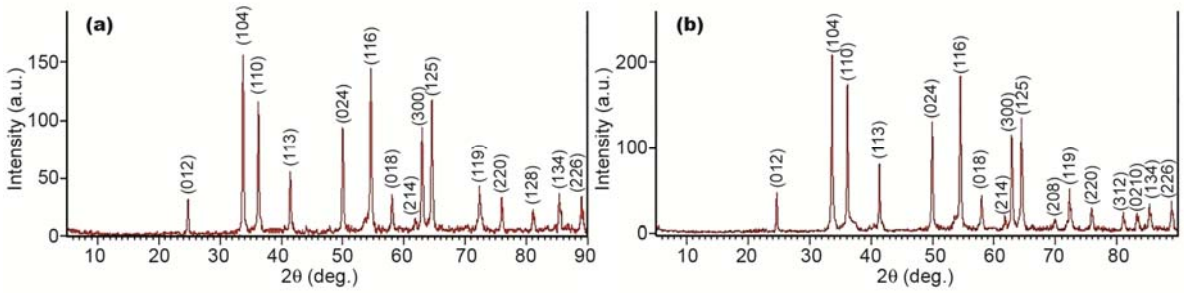

Fig. 1 — XRD patterns of nano sized α-Fe_2O_3 synthesized by wet high-energy ball-milling method. [(a) FW20; (b) FW40].

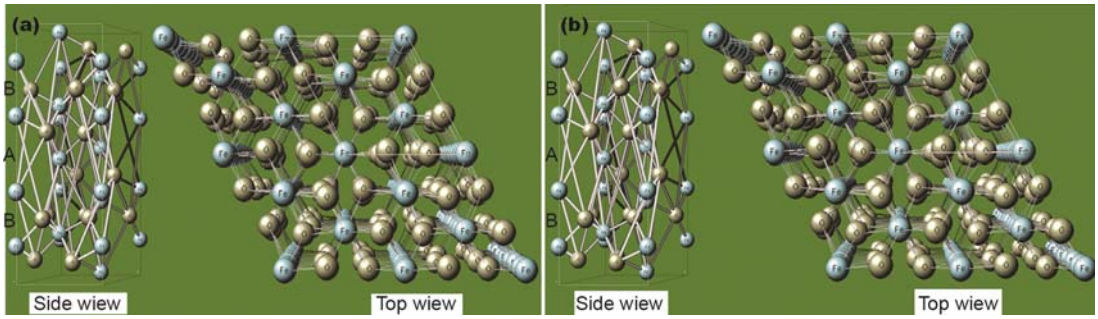

Fig. 2 — Schematic representation of a rhombohedral α-Fe_2O_3 NPs unit cell (side and top views). [(a) FW20; (b) FW40].

space group number 167) structure of hematite reflection (ICSD 01-089-0597) with lattice parameters of $a = b = 5.039$ Å, $c = 13.77$ Å, $\alpha = \beta = 90.00$, and $\gamma = 120.00$. Narrow sharp peaks suggest that both the synthesized samples are highly crystalline. Traces of characteristic peaks of other impurities like FeO, Fe_3O_4, and γ-Fe_2O_3 were not observed, indicating that only rhombohedral crystalline α-Fe_2O_3 NPs were obtained via the wet high-energy ball-milling method.

Based on Scherrer equation, the average crystallite size of the FW20 and FW40 NPs is calculated to be ~54 and ~48 nm, respectively[11]. Further, the present results show that α-Fe_2O_3 NPs without phase transformations were obtained after milling the microsize highly pure α-Fe_2O_3 powders for varying time periods (20 and 40 h).

Figure 2(a-b) shows the schematic representation of rhombohedral α-Fe_2O_3 NPs unit cell in 1×1×1 and 2×2×2 format (side and top views). Java Structure Viewer (Version1.08lite for Windows) program was used to model this crystalline structure[33]. The structural parameters and atomic coordinates used in this program are given in Table S1 (Supplementary Data). The oxygen and iron atoms sit on the (18e) and (12c) Wyckoff position, respectively. Figure 2(a-b) shows that there are two types of iron atom pairs, which are characterized by a large Fe-Fe distance (type A) and by a short Fe- Fe distance (type B) along the hexagonal axis. The values of larger Fe-Fe distance of the FW20 and FW40 NPs are 3.98 and 3.93 Å, respectively and values of shorter Fe-Fe distance of the FW20 and FW40 NPs are 2.88 and 2.94 Å, respectively. Thus, it is clear that a decrease in the size of α-Fe_2O_3 NPs led to a decrease in the larger Fe-Fe distance by about 0.5 Å, and increase in the shorter Fe-Fe distance by 0.6 Å.

FE-SEM images represented in Fig. 3(a-d) show irregular morphology with mean nanoparticle sizes of 56 and 51 nm of the FW20 and FW40 NPs, respectively. These results are in a good accordance with those from the XRD analysis (the crystalline sizes of about 54 nm and 48 nm for FW20 and FW40, respectively). The mean particle size values of α-Fe_2O_3 NPs varied strongly after 20 and 40 h ball-milling, and NPs ball-milled for 40 h were smaller than those milled for 20 h. Thus, based on the experimental results, it is clear that an increase in the ball-milling time led to a decrease in the size of α-Fe_2O_3 NPs.

Characterization of AP and AP+α-Fe_2O_3 nanocomposite particles

The FE-SEM images of AP and AP+α-Fe_2O_3 nanocomposite particles show that the AP particles are uniform with the mean diameter range of about 80–100 μm without any agglomeration (Fig. 4).

Also,

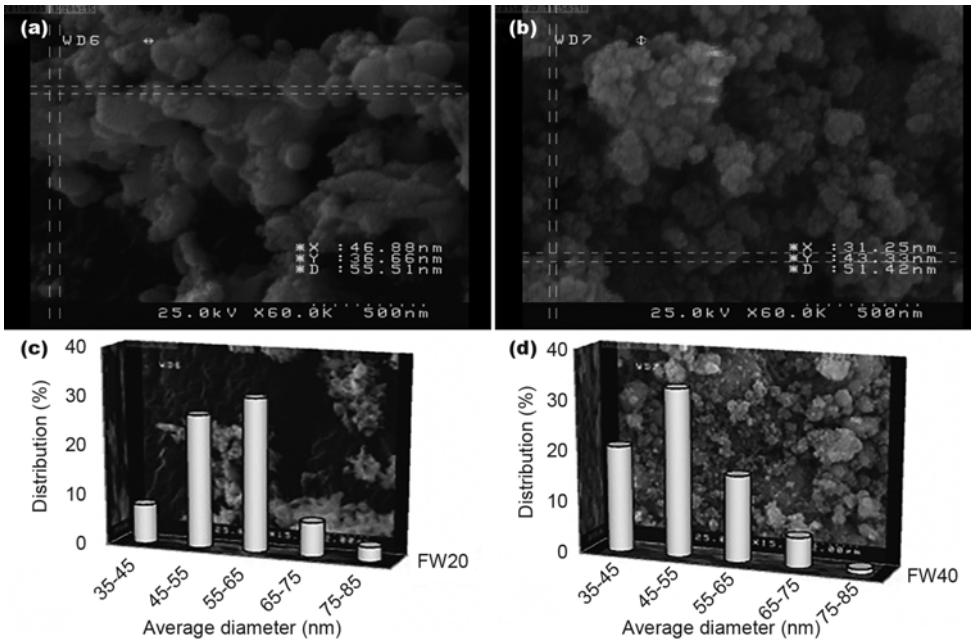

Fig. 3 — FE-SEM images of α-Fe_2O_3 NPs milled at (a) 20 h and (b) 40 h, and, particles size distribution histogram of α-Fe_2O_3 NPs milled at (c) 20 h and (d) 40 h.

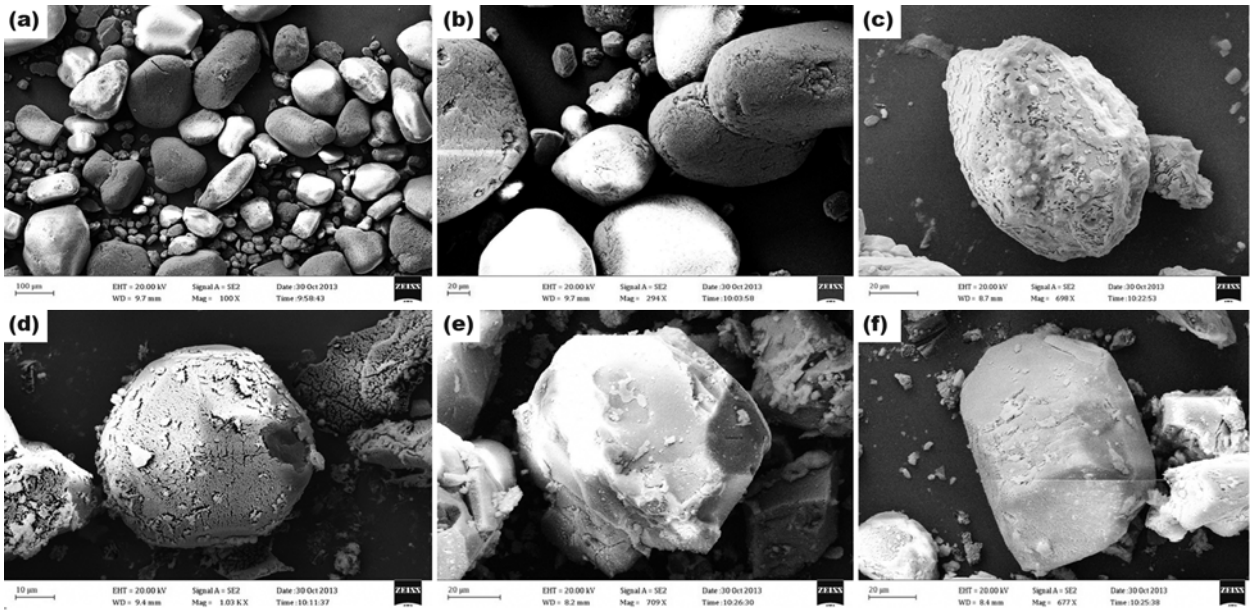

Fig. 4 — FE-SEM images of AP and AP+α-Fe_2O_3 samples. [(a-b) AP; (c) AP+2%FW20; (d) AP+5%FW20; (e) AP+2%FW40; (f) AP+5%FW40].

as can be seen in Fig. 4 (c-f), the α-Fe_2O_3 NPs (2 and 5 wt.%) are deposited on the surface of AP particles and inside the AP particles with high uniformity. Figure 4(c-f) shows that diameter of nanocomposites are 80-120 μm with nearly regular spherical particle morphology, without any agglomeration.

The EDS of AP and AP+5%FW40 samples confirmed the presence of α-Fe_2O_3 NPs in the nanocomposites. Figure 5 shows the EDS results of AP and AP+5%FW40 samples. Cl, O and N were

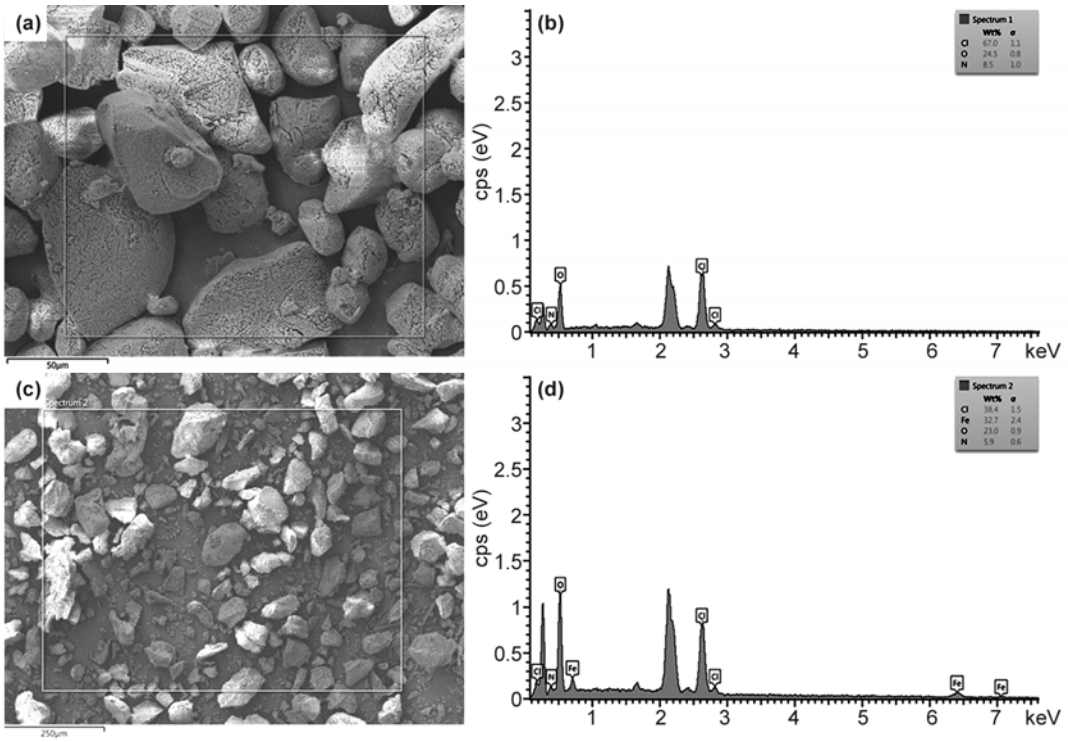

Fig. 5 — FE-SEM images of (a) AP, (b) EDS of the selected area of (a), (c) AP+5%FW40 nanocomposite and (d) EDS of the selected area of (c).

only present in the pure AP particles, which indicates that the purchased AP particles are essentially free from impurities. The FE-SEM and EDS data show that AP+α-Fe_2O_3 nanocomposites have been successfully prepared using solvent-nonsolvent method.

Catalytic activity of α-Fe_2O_3 NPs

TG and DSC analysis show that the thermal decomposition of AP at a heating rate of 10 °C min^{-1} was affected by α-Fe_2O_3 NPs. The mass loss of AP was investigated using TG curves of AP with α-Fe_2O_3 NPs (Fig. 6a). The TG curve of AP shows that the mass loss was in two steps, and the final thermal decomposition temperature was about 456.2 °C. On heating, AP first loses 35.4% of its mass at about 289.8 °C, i.e., low temperature decomposition (LTD). Complete decomposition of AP occurred almost at around 422.0 °C, i.e., high temperature decomposition (HTD)[7,26-32]. Also, it can be observed from the TG results that only one mass loss is detected in all the nanocomposites. The final thermal decomposition temperature of AP with 2%FW20, 5%FW20, 2%FW40 and 5%FW40 NPs was at about 416.7, 396.2, 378.7 and 366.4 °C, respectively. It is also observed that 5%FW40 NPs had the best catalytic performance on AP.

Furthermore, the DSC curves for thermal decomposition of AP showed three events (Fig. 6b). In the first event, the endothermic peak appeared at about 245.1 °C due to its phase transition from orthorhombic form to cubic form. In the second event (LTD), the exothermic peak at 289.8 °C was related to the partial decomposition of AP and formation of an intermediate product. In the third event (HTD), the main exothermic peak appeared at relatively higher temperature of 422.0 °C, indicating complete decomposition of the intermediate products[7,26-32].

The DSC curves for decomposition of AP in the presence of 2%FW20, 5%FW20, 2%FW40 and 5%FW40 NPs indicate significant differences in the decomposition patterns of AP. In the first event, the endothermic peaks at about 242–244 °C in all nanocomposites indicated a similar pattern; showing that α-Fe_2O_3 NPs had no effect on the phase transition temperature of AP. In the second stage, impressive changes in the exothermic peaks of AP decomposition were observed. The HTD process of AP disappeared and the DSC curves of all nanocomposites showed a greatly decreased peak temperature compared to HTD of pure AP. The HTD peak temperature depended on the particle size and wt.% of α-Fe_2O_3 NPs. It can be

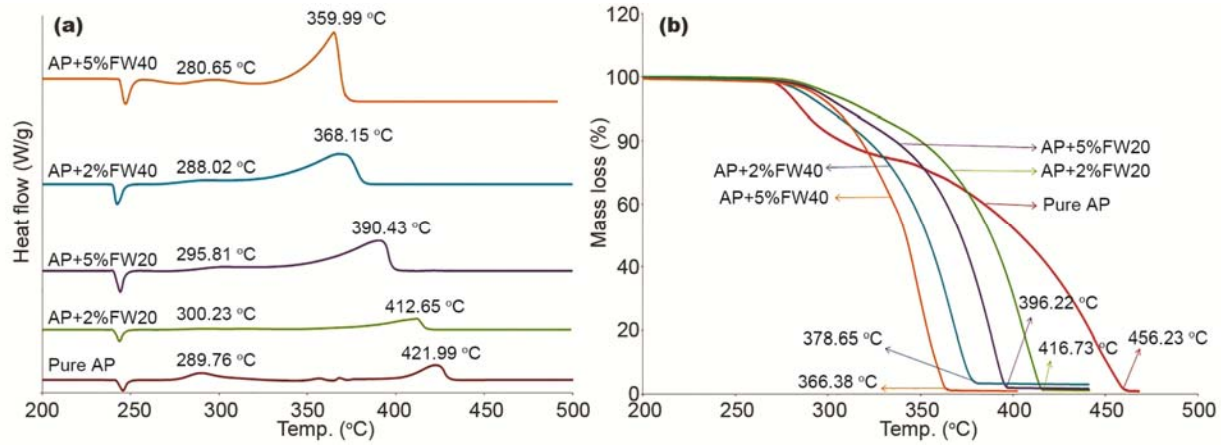

Fig. 6 — Thermal analysis of pure AP with and without α-Fe_2O_3 NPs. [(a) TG; (b) DSC; heating rate 10 °C min^{-1}; air atmosphere].

seen that the α-Fe_2O_3 NPs with a smallest particle size of 51 nm (5%FW40) lead to the lowest peak temperature of AP (360.0 °C). Also, when 2%FW40 was added to the AP, HTD shifted to 368.1 °C. The 2%FW20 has little effect on the decomposition temperature of AP. The HTD of AP in the presence of 2%FW20 only decreases by 9.4 °C. However, the HTD of AP with 5%FW20 decreases by 31.6 °C compared to that of the pure AP. Also, reduced α-Fe_2O_3 (56 to 51 nm) size indicated lower decomposition temperature than increased wt.% (2 to 5 wt.%) of α-Fe_2O_3 NPs. The above analysis showed that the FW40 NPs have higher catalytic activity compared with FW20 NPs. The above results further confirmed the discussion on the TG curves.

On addition of the additives 2%FW20, 5%FW20, 2%FW40 and 5%FW40 NPs, the heat of decomposition of AP increased by 170.5, 405.2, 444.2 and 528.1 J g^{-1}, respectively. On the other hand, smaller α-Fe_2O_3 (51–56 nm) size showed higher heat of decomposition than higher wt.% of α-Fe_2O_3 NPs. Thus, 5%FW40 NPs (ΔH = 1408.1 J g^{-1}) showed better catalytic performance for decomposition of AP than 2%FW20 (ΔH = 1050.5J g^{-1}), 5%FW20 (ΔH = 1285.2 J g^{-1}) and 2%FW40 (ΔH = 1324.2 J g^{-1}). This also shows that both FW20 and FW40 NPs had a promoting effect on thermal decomposition of AP.

The above results indicate that smaller size and the higher wt.% of the α-Fe_2O_3 NPs favor the decomposition of AP. Also, a comparative investigation of DSC results of AP decomposition with 2%FW20, 5%FW20, 2%FW40 and 5%FW40 NPs revealed that reduction in particle size (56 to 51 nm) of α-Fe_2O_3 NPs show better catalytic effect on the HTD of AP as compared to the increase in wt.% (2 to 5wt.%) of α-Fe_2O_3 NPs. Results of TG and DSC techniques demonstrated that the wet high-energy ball-milling synthesised α-Fe_2O_3 NPs exhibits excellent catalytic properties on AP thermal decomposition. Although, the α-Fe_2O_3 NPs synthesized using other methods are also efficient catalysts for the thermal decomposition of AP[7,26-32], the catalytic activity of α-Fe_2O_3 NPs synthesized herein via wet high-energy ball-milling method is comparable and have significant effects on thermal decomposition properties of AP particles. Comparison of catalytic activities of α-Fe_2O_3 nanoparticles, prepared by different methods as reported in literature, on thermal decomposition of treated ammonium perchlorate particles are given in Table S2 (Supplementary Data).

Kinetic and thermodynamic study

For a better understanding of the catalytic performance of α-Fe_2O_3 NPs, the relationship between decomposition temperature (T_m) and heating rate (β) for AP, AP+5%FW20 and AP+5%FW40 samples is shown in Table 1. Based on the exothermic peak temperatures calculated at four different heating rates of 5, 10, 15 and 20 °C min^{-1} in air atmosphere, kinetic parameters were obtained using the Kissinger, Boswell, Ozawa and Starink methods[34-38], by the following equation, $Y = \ln\frac{\beta}{T_m^Z} \approx -\frac{E_a}{RT_m} + C$, where C is constant, β is heating rate, T_m is the maximum peak temperature, and R is the gas constant. Here Z is a variable exponent, which assumes different values for different linearisation schemes. Z = 2, 1 and 0 are attributed to the Kissinger, Boswell and Ozawa methods, respectively. Starink, on the other hand, suggests that Z = 1.95, 1.92 or 1.8 may be adopted to get accurate values of kinetic parameters[37, 38].

In all methods, fitted plots showed an excellent linear correlation with coefficients *r* higher than 0.9623 (Supplementary Data, Fig. S1). Results indicate that among different values of *r* calculated for different methods, the highest value of *r* for pure AP and AP+5%FW40 samples corresponds to Ozawa method, while that for the AP+5%FW20 nanocomposites corresponds to Kissinger method. Calculated values of activation energy (E_a) and frequency factors (A) for AP, AP+5%FW20 and AP+5%FW40 samples are shown in Table 2.

The E_a values of the thermal decomposition of AP using Kissinger, Boswell, Ozawa and Starink (in 1.95, 1.92 and 1.8) methods are 280.7, 286.9, 292.9, 280.5, 280.7 and 282.9 kJ/mol, respectively. Also, the E_a values of the thermal decomposition of AP+5%FW20 nanocomposite using Kissinger, Boswell, Ozawa and Starink (in 1.95, 1.92 and 1.8) methods are 225.1, 225.3, 231.6, 222.2, 221.8 and 223.3 kJ mol^{-1}, respectively. Moreover, the E_a values of thermal decomposition of AP+5%FW40 nanocomposite using Kissinger, Boswell, Ozawa and Starink (in types 1.95, 1.92 and 1.8) methods are 93.8, 98.9, 103.5, 94.3, 94.3 and 95.2 $kJmol^{-1}$, respectively. The results of kinetic analysis clearly indicate that the addition of α-Fe_2O_3 NPs leads to reduction of A and E_a for AP thermal decomposition. Therefore, in the presence of α-Fe_2O_3 NPs, AP decomposition reaction needs to overcome a lower energy barrier compared to in the absence of α-Fe_2O_3 NPs. The decrease in the A of AP+5%FW20 and AP+5%FW40 nanocomposite is due to the lower probability of collisions between the reactants. Also, α-Fe_2O_3 NPs provide an alternative route for the reaction with a lower E_a. Since E_a is the least energy requirement to start a reaction, higher E_a values mean slower reactions[39]. Consequently, the

Table 1 — Effect of heating rate on the maximum temperature of decomposition (T_m) of AP, AP+5%FW20 and AP+5%FW40 samples

Heating rate (β) (°C min^{-1})	T_m (°C) AP (°C)	AP+5%FW20 (°C)	AP+5%FW40 (°C)
5	415.0	383.1	359.4
10	421.9	390.4	360.0
15	428.5	395. 6	368.1
20	435.0	397.1	375.5

Table 2 — Kinetic parameters for the decomposition of AP and AP with Fe_2O_3 NPs

Sample	Parameter	Kissinger	Boswell	Ozawa	Starink		
					Type-1.95	Type-1.92	Type-1.8
AP	E_a (kJ mol^{-1})	280.7±0.4	286.9±0.4	292.9±0.4	280.5±0.4	280.7±0.4	282.9±0.4
	log A (s^{-1})	20.9±0.4	21.4±0.4	21.8±0.4	20.9±0.4	20.9±0.4	21.1±0.4
	r	0.9986	0.9987	0.9989	0.9987	0.9986	0.9986
	-log *K* (s^{-1})	24.5	25.0	25.5	24.4	24.5	25.6
	Sp (kJ s mol^{-1})	13.4	13.4	13.43	13.42	13.4	13.4
	$\Delta G^{\neq}$ (kJ mol^{-1})	177.1	177.0	176.9	177.1	177.1	177.1
	$\Delta H^{\neq}$ (kJ mol^{-1})	274.9	281.1	287.1	274.7	274.9	277.1
	$\Delta S^{\neq}$ (J mol^{-1} K^{-1})	140.7	149.8	158.5	140.4	140.7	143.9
AP+5%FW20	E_a (kJ mol^{-1})	225.1±0.4	225.3±0.4	231.6±0.4	222.2±0.4	221.8±0.4	223.3±0.4
	log A (s^{-1})	17.5±0.4	17.5±0.4	18.0±0.4	17.3±0.4	17.2±0.4	17.4±0.4
	r	0.9668	0.9626	0.9645	0.9623	0.9635	0.9626
	-log *K* (s^{-1})	18.9	18.9	19.5	18.7	18.6	18.8
	Sp (kJ s mol^{-1})	12.86	12.9	12.9	12.8	12.9	12.8
	$\Delta G^{\neq}$ (kJ mol^{-1})	169.17	169.6	169.4	169. 7	169.7	169.6
	$\Delta H^{\neq}$ (kJ mol^{-1})	219.58	219. 8	226.1	216.7	216.3	217.8
	$\Delta S^{\neq}$ (J mol^{-1} K^{-1})	75.98	75. 6	85.4	70.8	70.3	72.6
AP+5%FW40	E_a (kJ mol^{-1})	93.8±0.4	98.9±0.4	103.5±0.4	94.3±0.4	94.3±0.4	95.2±0.4
	log A (s^{-1})	7.2±0.4	7.6±0.4	8.0±0.4	7.2±0.4	7.2±0.4	7.3±0.4
	r	0.9873	0.9882	0.9894	0.9868	0.9868	0.9875
	-log *K* (s^{-1})	8.0	8.4	8.7	8.1	8.1	8.1
	Sp (kJ s mol^{-1})	13.0	13.0	11. 9	13.1	13.1	13.0
	$\Delta G^{\neq}$ (kJ mol^{-1})	165.7	165.4	165.1	165. 7	165.7	165.7
	$\Delta H^{\neq}$ (kJ mol^{-1})	88.5	93.6	98.2	89.0	89.0	89.9
	$\Delta S^{\neq}$ (J mol^{-1} K^{-1})	121. 9	113.3	105.7	121.1	121.1	119.7

thermal decomposition reactions of AP+5%FW20 and AP+5%FW40 nanocomposites are generally very fast.

In all methods, assuming a first-order kinetic rate law for decomposition, the rate constant (K) of the reaction given by[40] $\log K = \log A - \frac{E_a}{2.3RT}$ was calculated at 50 °C. The rate constant of the decomposition reactions are listed in Table 2. The K for AP is less than that of AP+5%FW20 and AP+5%FW40 nanocomposites at the selected temperature. Compensation parameter (Sp = E_a/logA) was chosen to describe the reaction ability of the AP, AP+5%FW20 and AP+5%FW40 samples. The smaller the value of Sp, the better the catalytic efficiency of α-Fe_2O_3 NPs on thermal decomposition temperatures of AP[41]. Analysis of the data in Table 2 showed that after adding 5%FW20 and 5%FW40 NPs to AP, Sp value was significantly less than that of pure AP, which was the direct evidence for the high catalytic activity of 5%FW20 and 5%FW40 NPs.

The values of thermodynamic parameters of activation Gibbs free energy ($\Delta G^{\#}$), enthalpy ($\Delta H^{\#}$) and Entropy ($\Delta S^{\#}$) were calculated from the following equations for detailed study of the mechanism[42]. Table 2 shows the calculated values of thermodynamic parameters for AP, AP+5%FW20 and AP+5%FW40 samples. The results show that the values of $\Delta H^{\neq}$ are in agreement with E_a values obtained by Kissinger, Boswell, Ozawa and Starink methods. Also, the addition of α-Fe_2O_3 NPs in AP leads to a significant reduction in the values of thermodynamic parameters of $\Delta G^{\#}$, $\Delta H^{\#}$ and $\Delta S^{\neq}$. Comparing the results of the application of the Kissinger, Boswell, Ozawa and Starink methods, it was observed that all the methods showed the same trend of the kinetic and thermodynamic parameters and are almost close to each other. Thus, these methods are suitable for estimating kinetic and thermodynamic parameters.

Conclusions

α-Fe_2O_3 NPs were synthesized via wet high-energy ball-milling method and characterized by XRD and FE-SEM techniques. The catalytic performance of syntheses α-Fe_2O_3 NPs on the thermal decomposition of AP was investigated. TG and DSC measurements confirmed that noticeable catalytic performance effects were observed on adding 2%FW20, 5%FW20, 2 %FW40 and 5%FW40 of NPs. The 5%FW40 NPs nanocomposite showed the highest catalytic performance for the reduction of decomposition temperature of AP particles (by 62 °C). Also, it was found that the decomposition temperature and heat of decomposition were strongly dependent on the mean particle size and wt.% of the prepared α-Fe_2O_3 NPs. Finally, kinetics and thermodynamics calculations indicated that the addition of α-Fe_2O_3 NPs led to the reduction of apparent E_a, A, Sp, $\Delta G^{\#}$, $\Delta H^{\#}$ and $\Delta S^{\neq}$ of the thermal decomposition reaction of AP particles.

Supplementary Data

Supplementary data associated with this article, viz.; Tables S1 & S2, and Fig. S1 are available in the electronic form at http://www.niscair.res.in/jinfo/ijca/IJCA_56A(06)592-600_SupplData.pdf.

References

1 Davenas A, *Solid Rocket Propulsion Technology*, (Pergamon Press, Oxford) 1993, p. 443.

2 Sutton G P & Biblarz O, *Rocket Propulsion Elements*, (Wiley, USA) 2010, p. 435.

3 Chunwei W, Kyl S, Snehaunshu C, Guoqiang J, Lei Z & Michael R Z, *Adv Funct Mater*, 22 (2012) 78.

4 Hosseini S G, Pourmortazavi S M & Hajimirsadeghi S S, *Combust Flame*, 141 (2005) 322.

5 Fathollahi M, Pourmortazavi S M & Hosseini S G, *Combust Flame*, 138 (2004) 304.

6 Zou M, Wang X, Jiang X & Lu L, *J Solid State Chem*, 213 (2014) 235.

7 Hosseini S G, Ahmadi R, Ghavi A & Kashi A, *Powder Technol*, 278 (2015) 316.

8 Zhang Y, Wang N, Huang Y, Wu W, Huang C & Meng C, *Ceram Int*, 40 (2014) 11393.

9 Wang J G, Jin L N, Qian X Y & Dong M D, *J Nanosci Nanotechnol*, 16 (2016) 8635.

10 Jia Z, Ren D, Wang Q & Zhu R, *Appl Surf Sci*, 270 (2013) 312.

11 Dubey B L, Singh N B, Srivastava J N & Ojha A K, *Indian J Chem*, 40A (2001) 841.

12 Ayoman E & Hosseini S G, *J Therm Anal Calorim*, 123 (2016) 1213.

13 Hu H, Ge X, Zheng Q & Deng C, *Korean J Chem Eng*, 11 (2015) 2335.

14 McDonald B A, Rice J R & Kirkham M W, *Combust Flame*, 161 (2014) 363.

15 Wheeler D A, Wang G, Ling Y, Li Y & Zhang J Z, *Energy Environ Sci*, 5 (2012) 6682.

16 Gurlo A, Sahm M, Oprea A, Barsan N & Weimar U, *Sensors Actuators B*, 102 (2004) 291.

17 Liu Q, Cui Z M, Ma Z, Bian S W, Song W G & Wan L J, *Nanotechnology*, 18 (2007) 385065.

18 Xu Y Y, Rui X F, Fu Y Y & Zhang H, *Chem Phy Lett*, 410 (2005) 36.

19 Kudo A & Miseki Y, *Chem Soc Rev*, 38 (2009) 253.

20 Sonavane S U, Gawande M B, Deshpande S S, Venkataraman A & Jayaram R V, *Catal Commun*, 8 (2007) 1803.

21 Chin A B & Yaacob I I, *J Mater Process Technol*, 191 (2007) 235.

22 Huang Y, Chen W, Zhang S, Kuang Z, Ao D, Alkurd N R, Zhou W, Liu W, Shen W & Li Z, *Appl Surf Sci*, 351 (2015) 1025.
23 Tang B, Wang G, Zhuo L, Ge J & Cui L, *Inorg Chem*, 45 (2006) 5196.
24 Pourghahramani P & Forssberg E, *Powder Technol*, 178 (2007) 30.
25 Bid S, Banerjee A, Kumar S, Pradhan S K, Dec U & Banerjee D, *J Alloys Comp*, 326 (2001) 292.
26 Patil P R, Krishnamurthy V N & Joshi S S, *Propellants Explos Pyrotech*, 31 (2006) 442.
27 Joshi S S, Patil P R & Krishnamurthy V N, *Def Sci J*, 58 (2008) 721.
28 Ma Z, Li F & Bai H, *Propellants Explos Pyrotech*, 31 (2006) 447.
29 Kapoor I P S, Srivastava P & Singh G, *Propellants Explos Pyrotech*, 34 (2009) 351.
30 Ma Z, Wu R, Song J, Li C, Chen R & Zhang L, *Propellants Explos Pyrotech*, 37 (2012) 183.
31 Song L, Zhang S, Chen B, Ge J & Jia X, *Colloids Surf A: Physicochem Eng Asp*, 360 (2010) 1.
32 Zhang Y, Liu X, Nie J, Yu L, Zhong Y & Huang C, *J Solid State Chem*, 184 (2011) 387.
33 *http://www.jcrystal.com/steffenweber/JAVA/JSV/jsv.html*.
34 Kissinger H E, *Anal Chem*, 29 (1957) 1702.
35 Boswell P G, *J Therm Anal*, 18 (1980) 353.
36 Ozawa T, *B Chem So Jpn*, 38 (1965) 1881.
37 Starink M J, *Thermochim Acta*, 404 (2003) 163.
38 Starink M J, *Therrnochim Acta*, 288 (1996) 97.
39 Ceylan S & Topçu Y, *Bioresour Technol*, 156 (2014) 182.
40 Eslami A & Hosseini S G, *J Therm Anal Calorim*, 104 (2011) 671.
41 Wang W, Chen S & Gao S, *Eur J Inorg Chem*, 2009 (2009) 3475.
42 Eslami A, Hosseini S G & Pourmortazavi S M, *Fuel*, 87 (2008) 3339.